Full length article

Metallurgy of high-silicon steel parts produced using Selective Laser Melting

Michele Garibaldi, Ian Ashcroft*, Marco Simonelli, Richard Hague

Additive Manufacturing and 3D Printing Research Group, Faculty of Engineering, The University of Nottingham, Nottingham NG7 2RD, United Kingdom

ABSTRACT

The metallurgy of high-silicon steel (6.9%wt.Si) processed using Selective Laser Melting (SLM) is presented for the first time in this study. High-silicon steel has great potential as a soft magnetic alloy, but its employment has been limited due to its poor workability. The effect of SLM-processing on the metallurgy of the alloy is investigated in this work using microscopy, X-Ray Diffraction (XRD) and Electron Backscatter Diffraction (EBSD). XRD analysis suggests that the SLM high-silicon steel is a single ferritic phase (solid solution), with no sign of phase ordering. This is expected to have beneficial effects on the material properties, since ordering has been shown to make silicon steels more brittle and electrically conductive. For near-fully dense samples, columnar grains with a high aspect ratio and oriented along the build direction are found. Most importantly, a <001> fibre-texture along the build direction can be changed into a cube-texture when the qualitative shape of the melt-pool is altered (from shallow to deep) by increasing the energy input of the scanning laser. This feature could potentially open the path to the manufacture of three-dimensional grain-oriented high-silicon steels for electromechanical applications.

© 2016 The Authors. Published by Elsevier Ltd on behalf of Acta Materialia Inc. This is an open access article under the CC BY license (http://creativecommons.org/licenses/by/4.0/).

1. Introduction

Over the past few years, Additive Manufacturing (AM) technologies have been enjoying an ever-growing success, thanks to the unrivalled design freedom they offer for the fabrication of both plastic and metallic components [1]. In particular, Selective Laser Melting (SLM) is emerging across a broad range of sectors, including automotive, medical and aerospace, for the creation of functional metallic parts. SLM achieves densities comparable to the bulk material by applying a high-power laser beam to a layer of metallic powder, according to the data contained inside the CAD file of the part. The laser energy fully melts the powders together, consequently creating solid metal upon cooling.

The use of laser-based AM has been investigated for processing a range of metallic materials for structural applications, including stainless and carbon steels, as well as a number of titanium, cobalt and aluminium alloys [2–5]. However, the potential of this manufacturing technology for applications other than structural is almost unexplored. A significant example in this regard is represented by those materials with ferromagnetic properties, such as soft and permanent magnets. Applications that rely upon such materials include the large family of devices that transform electrical energy into mechanical energy, such as motors, and from mechanical to electrical, such as AC generators. The contribution of Zhang et al. [6] is the sole example of the application of SLM for processing a soft magnetic alloy. In their paper, the authors showed the beneficial effect of microstructure refinement by SLM-processing on the DC soft magnetic properties of Permalloy. The lack of further reference on the topic indicates a gap in the literature, as it seems that the successful processing of magnetic core materials through AM has the potential to open the path to a new generation of designs for highly performing electromechanical devices.

An important class of soft magnetic materials are silicon steels, which are iron alloys with silicon in concentrations ranging from 2–7%wt. Within the family of silicon steels, Fe-6.5%Si alloys have a high potential in magnetic device applications due to their high electrical resistivity, near-zero magnetostriction, and low magnetocrystalline anisotropy [7]. Despite their high potential, these alloys are rarely used in commercial applications because of their very limited ductility, which results in poor workability. A recent technique developed by JFE Steel employs a chemical vapour deposition treatment to add silicon once the lamination has been created [8]. The two 6.5%Si lamination types obtained through this

* Corresponding author.
  E-mail address: Ian.Ashcroft@nottingham.ac.uk (I. Ashcroft).

technique, namely JNEX and JNHF, represent the only examples of commercialised high-silicon electrical steels. Other attempts of high-silicon steel processing have been explored in the literature, in the form of powder cores [9], cast strips [10] and electron-beam physical vapour deposited sheets [11].

The tool-free nature of SLM could offer an alternative manufacturing route for processing near-fully dense high-silicon steel parts with unique microstructural properties. Importantly, owing to the additive nature of the SLM process and the thermal history the material experiences, a crystallographic texture can be induced. A number of contributions have shown that SLM processing can create interesting crystallographic features [12,13]. In Refs. [12], a high power laser was employed to produce highly anisotropic stainless steel with strong morphological and crystallographic textures. In Refs. [13], it was shown that changing the scan strategy (i.e., the path followed by the processing laser) affects the crystallographic texture of AlSi10 Mg. The authors showed that a strong fibre texture obtained by scanning every layer using unidirectional vectors could be changed into a weak cube texture when scan vectors rotated by 90° within and between layers were employed. As regards to the silicon steels, controlling the crystallographic texture is very attractive in a number of applications, since the <001> crystallographic direction is the "easy axis" of magnetisation [14]. While cold rolling is a widespread method to obtain laminations with strong <001> texture along the rolling direction and <101> texture along the transverse and normal directions (cube-on-edge or Goss texture, as explained in Ref. [15]), a manufacturing process able to produce cube-textured parts could potentially extend the applicability range of the alloy.

The aim of this paper is to show that three-dimensional high-silicon steel parts can be manufactured using SLM and to present their metallurgy. First, the contribution of laser energy density is studied with the goal of promoting part densification. Then, the microstructure is investigated in terms of solid phase formation, grain size and morphology, as well as crystallographic texture.

2. Experimental methods

2.1. Sample manufacturing and post-processing

High-silicon steel powder with approximately 6.9% wt. Si (refer to Table 1 for a list of the alloying elements) was provided by LPW Technology Ltd., Runcorn, UK. It was experimentally verified that the powder particles are approximately spherical in shape with a symmetrical size distribution centred at 35 μm. Particle size ranges from approximately 10 μm−60 μm. This is in fairly good agreement with the range declared by the supplier (15 μm-45 μm). Powder was first dried at 60 °C for 120 min and then processed to produce test samples using a Realizer SLM-50 (Realizer GmbH, Borchen, Germany), equipped with a continuous 100 W yttrium fibre laser (YLM- 100-AC). The SLM process was conducted under an Argon atmosphere with an oxygen level below 0.4%. The platform on which the specimens were built was kept at 200 °C to maintain the part at an elevated temperature so as to reduce thermal expansion gradients. Standard cubic samples of dimensions 5 × 5 × 5 mm were produced for analysing the porosity, crack formation and the

microstructures.

As regards the manufacturing process, the main SLM parameters are defined in Fig. 1. In the present study, laser power (P), laser beam focus position, hatch-spacing, scan distance and layer thickness were kept constant. The values chosen for these parameters are those recommended by the Realizer SLM-50 manufacturer for processing stainless steel powders. Among the alloys routinely processed using the Realizer SLM-50 (which include Co-Cr, AlSi10 Mg and Ti6Al4V), the thermal and optical properties of atomised stainless steel powder are expected to be the closest to those of silicon steel, owing to the similar iron content in the two alloys. The scan speed (v) was varied in order to study the effects of the energy input $E = P/v$ on the material properties. As regards the scan strategy, each layer was scanned once using vectors oriented along either the X-axis (scan direction-x, SD_x) or the Y-axis (scan direction-y, SD_y), alternatively. This strategy is referred to as bidirectional X-Y in the present manuscript. Table 2 summarises the process parameter values used in this study. For simplicity, each sample is identified by the values of energy input E used to build it. For instance, the sample manufactured using $P = 70$ W and $v = 0.5$ m/s, which corresponds to an energy input $E = 140$ J/m is referred to as S_{140}.

2.2. Study of sample metallurgy

In order to investigate the porosity and microstructural features, the manufactured 5 × 5 × 5 mm cubic samples were cut along three perpendicular planes, parallel to the cube faces. The test specimens were cross-sectioned, mounted, and polished. The relative porosity was determined from the optical micrographs of the vertical cross-sections of the samples. An Eclipse LV100ND microscope (Nikon, Tokyo, Japan) was used to obtain the micrographs. As a quantitative means of assessing crack formation, the cumulative crack length (c.c.l.) was used. This parameter was defined as c.c.l. $= 1/n \sum \sum l_{ij}$, where l_{ij} is the length of the jth crack on the ith polished sample surface and n is the total number of sample surfaces considered for each sample. To achieve repeatability, for each test sample a minimum of four to a maximum of six cross-sectional optical micrographs were acquired and analysed using the open source image processing software ImageJ [16].

A TM3030 scanning electron microscope (SEM) by Hitachi, Tokyo, Japan, with a 20 kV accelerating voltage and backscattered electron detector was used to evaluate the microstructures. In order to assess grain morphology and size, SEM micrographs were acquired from both the horizontal (top) and vertical (front and side) cross-sections of each sample. In order to visualise melt-pool boundaries, the sample surfaces were etched by exposing them to a solution of 2% Nital for 40s−60s. In addition, the SEM was equipped with an Energy Dispersive X-ray (EDX) detector that was used to assess the distribution of the main alloying elements in the built parts.

Solid phase distribution and lattice parameter were measured by XRD using a D500 diffractometer (Siemens, Munich, Germany) with CoKα radiation. Diffraction peaks in the range 2θ = [25°, 90°] were considered for determining the solid phase. The acquisition conditions were step size $\Delta\theta = 0.05°$ and step time $t = 8s$. Background removal and Kα2 radiation stripping were performed before peak indexing using Diffrac. EVA software (Bruker, Billerica, Massachusetts). The lattice parameter was measured from the sixth diffraction peak (corresponding to diffraction plane family {222}) in order to achieve high accuracy. The acquisition conditions were step size $\Delta\theta = 0.02°$ and step time $t = 30$ s.

For the analysis of the crystallographic texture intensity using EBSD, a Nova 600 Nanolab Dualbeam FIB/FEG-SEM system (FEI, Hillsboro, Oregon) was employed. EBSD maps and pole figures were

Table 1
Alloying elements concentration range of the employed high-silicon steel powders according to supplier LPW Technologies Ltd.

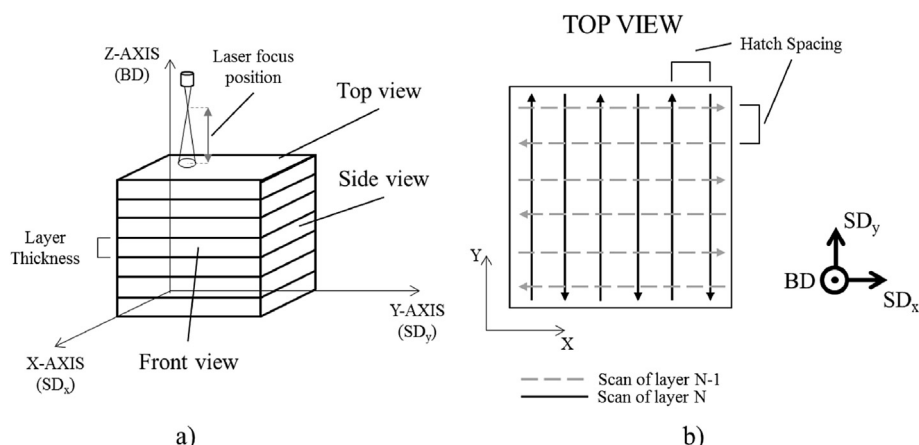|	Element				
	Si	Mn	C	P	O
Concentration (%wt.)	6.9	0.05	0.01	0.009	0.0065

Fig. 1. Overview of the SLM processing parameters and laser scan strategy. The build (BD) and scan directions (SD_x and SD_y) are indicated with respect to the sample coordinates. In (a) the different views of the cubic sample are indicated and the definitions of layer thickness and layer focus position are represented. Top view of the sample with the bidirectional scan vectors is provided in (b).

Table 2
The SLM process parameters employed for manufacturing the test samples of high-silicon steel.

SLM Parameter	Values (units)
Laser Beam Focus Position	13.1 (mm)
Hatch Spacing	60 (μm)
Layer thickness	25 (μm)
Laser Power (P)	70 (W)
Laser Scan Speed (v)	1−0.5−0.25−0.167−0.125 (m/s)
Scan Strategy	Bidirectional X-Y

acquired for front, side and top views of each sample, in order to achieve repeatability of the results. The scanning step size for the EBSD map was 2 μm. Grains were defined by a misorientation angle larger than 5°. The average confidence index of the EBSD measurements was calculated to be around 0.70. The obtained data was analysed using microstructural data analysis software TSL OIM (Ametek Inc, Berwyn, Pennsylvania). The final EBSD images were obtained by combining the transparent orientation maps with the corresponding image quality maps, so that the grain boundaries are visible.

3. Results

3.1. Study of densification and crack formation

The optical micrographs in Fig. 2A present the effects of the laser energy input on porosity and pore morphology. In Fig. 2B, the histograms show the quantitative evolution of sample porosity (in terms of percentage porosity) and crack formation (in terms of c.c.l.) with increasing laser energy input. The results show that the samples obtained with laser energy inputs $E < 280 \ J/m$ are characterised by large pores of irregular shape. Increasing the energy input at 280 J/m promotes reduction of the irregular pores, but induces crack formation. With $E \geq 420 \ J/m$, small bubble-like voids (i.e., spherical pores) appear, while crack formation is promoted, as suggested by the increasing trend of the c.c.l. parameter.

Given the results presented in Fig. 2, samples S_{140} and S_{280} were considered to provide the best compromise in terms of part densification and crack formation. Sample S_{140} was crack-free and presented a percentage porosity of 1.56 ± 0.21, whereas for sample S_{280} percentage porosity was found to achieve a value of 0.50 ± 0.06 with the largest micro-crack presenting a maximum width <20 μm.

The SEM micrographs in Fig. 2B provide an insight into the two main types of porosities observed in the processed parts and their relationship with the qualitative shape of the melt-pool. Some of the melt-pool boundaries in Fig. 2B are highlighted by the dashed and solid lines, depending on whether the corresponding laser scan tracks are aligned with the SD_x or SD_y, respectively. While the irregular pores are normally located at the intersection between wide, shallow melt-pools (left micrograph in Fig. 2B), the spherical pores are observed at the bottom of deeper, protuberant melt-pools (right micrograph in Fig. 2B).

3.2. Study of solid phase formation

The results obtained from XRD analysis (Fig. 3) suggest that the microstructure of both the powder and SLM-processed samples is characterised by a single bcc-phase (i.e., α-ferrite), owing to the high silicon content that suppresses γ-phase formation. The SEM micrograph and EDX analysis reported in Fig. 4 for sample S_{280} support the XRD data in that the compositional range for iron and silicon corresponds to that expected for the solid solution.

With regards to the structural state of the ferritic phase, the amplified versions of the XRD spectrogram in Fig. 3A show no superstructure lines. This suggests that coarse areas of ordered phases B_2 and DO_3 are not present in the microstructure. Further evidence of the absence of significant phase ordering in the SLM samples is provided by the analysis of the bcc lattice parameter reported in Fig. 3B. It is well known from the literature [7] that the lattice parameter of the Fe-Si system decreases linearly with increasing Si content. The slope of the function describing the linear relationship changes abruptly at 5%Si, owing to the start of atom configuration ordering.

The lattice parameter for the SLM high-silicon steel samples considered in Fig. 3B lies below the reference value for pure bcc-Iron (upper limit) and well above that for cast Fe-6.7%Si, where superstructure lines in the XRD spectrum are known to appear due to ordering initiation [7]. The value for the unprocessed atomised powders is found to be smaller than for any of the processed samples, but still above the value for cast Fe-6.7%Si. However, it is found that the lattice parameter of the SLM samples linearly decrease with decreasing laser scan speed (i.e., with increasing energy input), suggesting that phase reorganisation, although probably limited, might take place and is influenced by the thermal history of the samples during SLM processing.
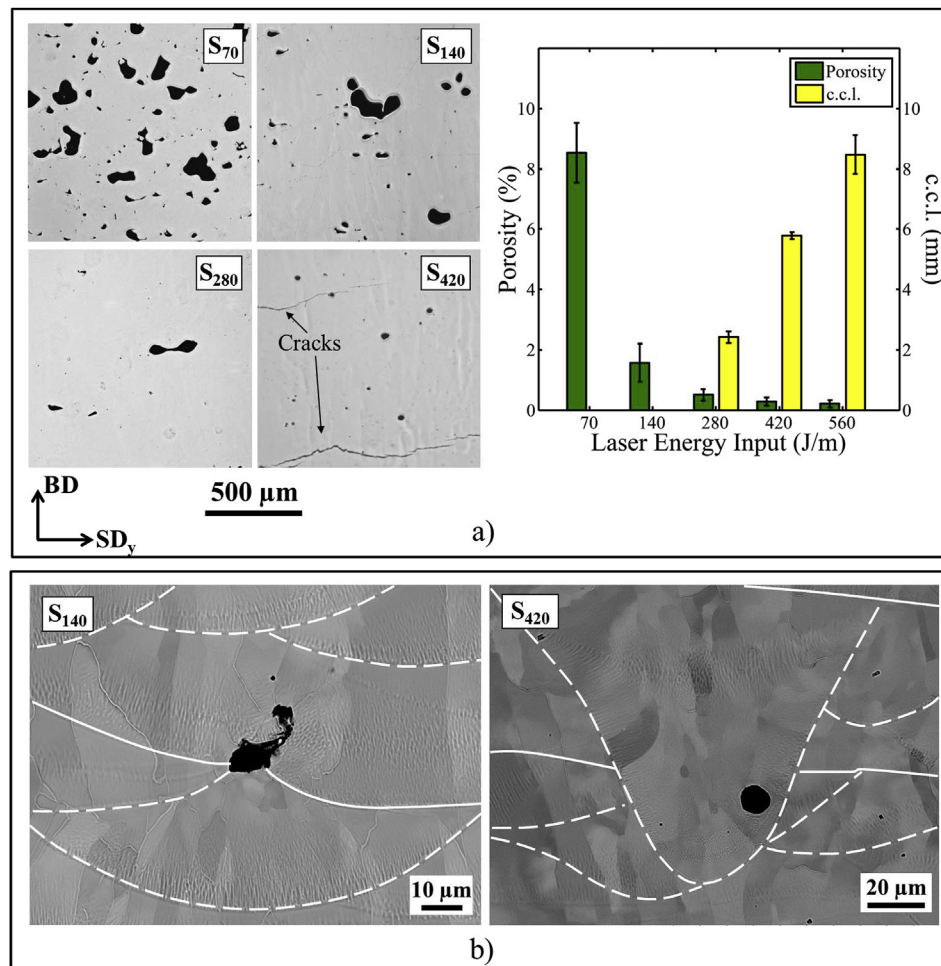
Fig. 2. Effect of processing laser energy input on sample porosity. In a) the optical micrographs of different SLM samples are shown (left), alongside the values of percent porosity and c.c.l. plotted against laser energy input (right). The SEM micrographs in b) show two examples of irregular (left) and spherical pores (right). The dashed and solid lines indicate the transversal and longitudinal melt-pool cross-sections, respectively.

3.3. Study of microstructures

The SEM micrographs in Figs. 5 and 6 provide insights into the microstructural features of samples S_{140} and S_{280} for the top and front views (please note that the microstructures for the front view of the samples were also found for the side view and are therefore not shown here). Fig. 5 shows that the grain boundaries of the processed samples are not always clearly identifiable. However, in the vertical plane the grains appear to present an overall columnar morphology and are more or less oriented along the BD, suggesting that epitaxial growth of the grains takes place, according to a grain selection process in which grains whose "easy growth" directions (the <001> family for the bcc system) are oriented along the direction of solidification outgrow the less optimally oriented grains. For sample S_{280} the grains appear more elongated and in some cases span several hundred microns along the BD.

As regards the horizontal plane of the samples, the two micrographs at bottom of Fig. 5 show that the grain structure of sample S_{280} is coarser than that of sample S_{140}. Furthermore, the grains are equiaxed for sample S_{140}, whereas the grain structure of sample S_{280} is more heterogeneous. In particular, two grain morphologies are of interest in the higher energy input sample. Regions of fine, equiaxed grains (indicated by the letter C in Fig. 5) are found in correspondence of the scan track centreline. Adjacent to the centrelines (which are not always visible owing to melt-pool overlap),

regions of coarser, elongated grains (identified by the letter E in Fig. 5) are observed.

From the SEM images in Fig. 5 the melt-pool boundaries are also visible and appear to significantly affect the grain structures of the two samples considered. In the vertical plane, the transversal melt-pool cross-sections of sample S_{140} are shallow and flat, whereas in S_{280} both shallow and protuberant melt-pools are observed, in similar proportions. Since melt-pool shape determines the orientation of the heat flow and consequently the solidification patterns, it significantly affects grain orientation. In this regard, the front view of the samples in Fig. 5 suggest that in sample S_{140} the longitudinal melt-pool cross-sections are more irregular than in sample S_{280} and this causes the formation of a more heterogeneous grain orientation in the former sample.

In order to understand how shallow and protuberant melt-pools affect the grain structures, the SEM micrographs in Fig. 6 offer a closer look at the two types of melt-pool shapes for the front view of the samples. Inside both melt-pool types, the grains are formed by cellular-dendritic solidification substructures that appear as thin stringy features stretching parallel to the longitudinal axis of the grains. The fact that the cellular substructures become visible upon etching suggests that excess-solute partitioning into the cellular spacings has occurred during solidification. The orientations of the solidification substructures in different regions of the melt-pools are indicated by the arrows in Fig. 6. Inside the shallow melt-
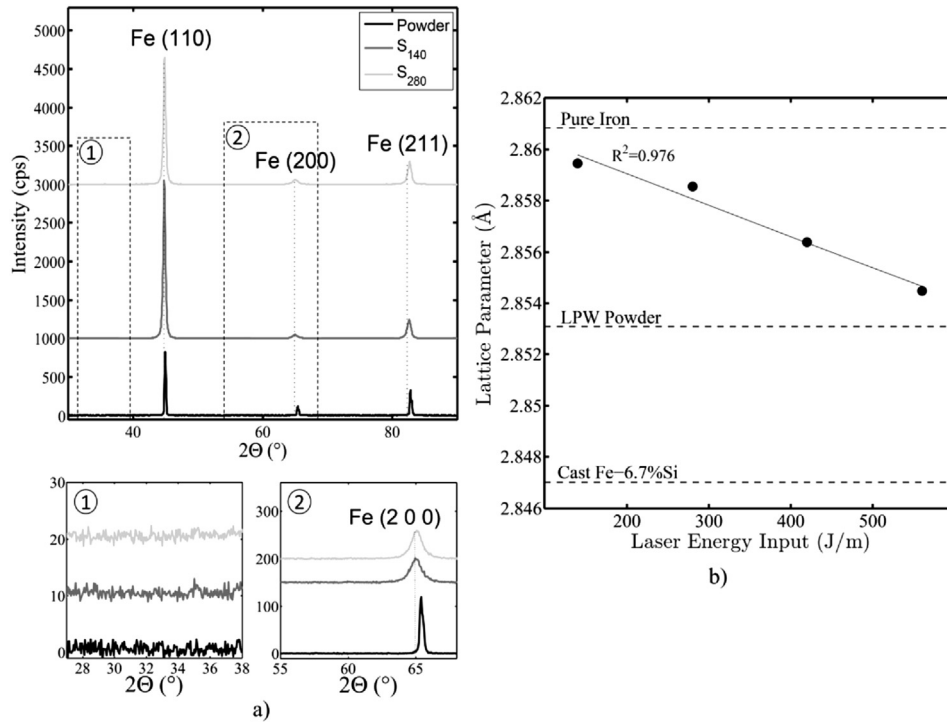
Fig. 3. XRD analysis of SLM high-silicon steel. In a), the main and amplified plots show the XRD spectra for powder and samples S_{140} and S_{280}. In b) the lattice parameters are shown for four samples processed using different energy inputs, the powder and the reference values of pure iron and cast Fe-6.7%Si from Ref. [7].
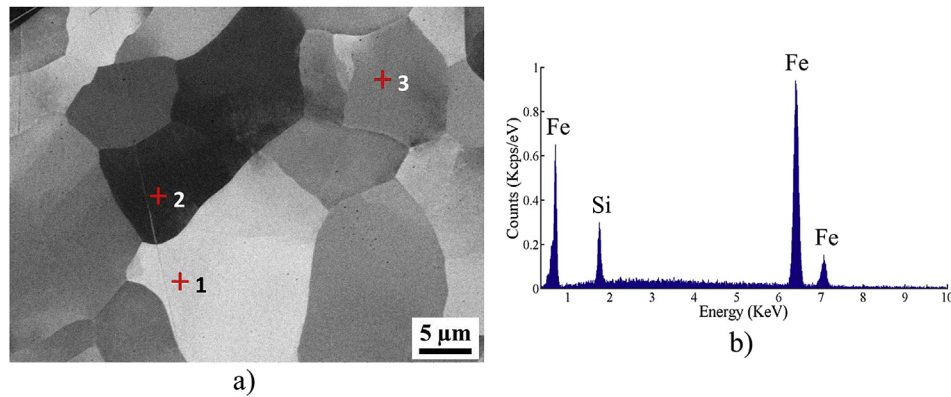

Region	1	2	3
Fe (wt%)	93.15	91.75	93.32
Si (wt%)	6.85	8.25	6.68

c)

Fig. 4. Grain composition of sample S_{280} measured by EDX. SEM image of the investigated region (a), EDX spectrum corresponding to region 1 (b), and chemical composition in the three regions under exam (c).

pools (Fig. 6C and D) the solidification substructures grow mainly parallel to the BD, regardless of the location within the melt-pool, owing to the almost vertical orientation of the solidification front normal.

In the protuberant melt-pools (Fig. 6A and B) the growth path orientation depends on the location inside the melt-pool. In correspondence of the melt-pool centreline the cellular substructures and corresponding grains are oriented along the BD and grow epitaxially. In the regions adjacent to the centreline, growth has

mainly occurred towards the centreline according to the inclination of the melt-pool boundaries. The grains in this region of the melt-pool correspond, in the horizontal plane of the sample, to the elongated structures identified by the letter E in the image at the bottom-right of Fig. 5. In these regions epitaxial growth along the BD should be hindered by the inclination of the melt-pool boundary with respect to the BD. However, since the lateral melt-pool boundaries are oriented more or less along the BD in the protuberant portion of the melt-pool, the cellular-dendrites growing
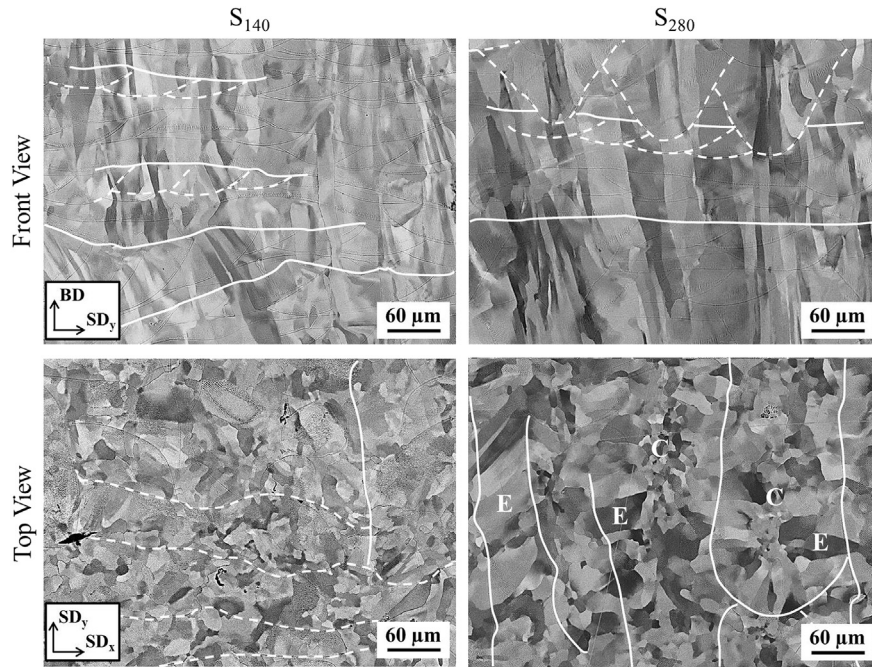
Fig. 5. SEM micrographs for the top and front views of samples S_{140} and S_{280}. The boundaries of some of the melt-pool cross-sections are highlighted by the dashed and solid lines, depending on the orientation. In the top view of sample S_{280} the letter E and C indicate regions of elongated and equiaxed grains, respectively.
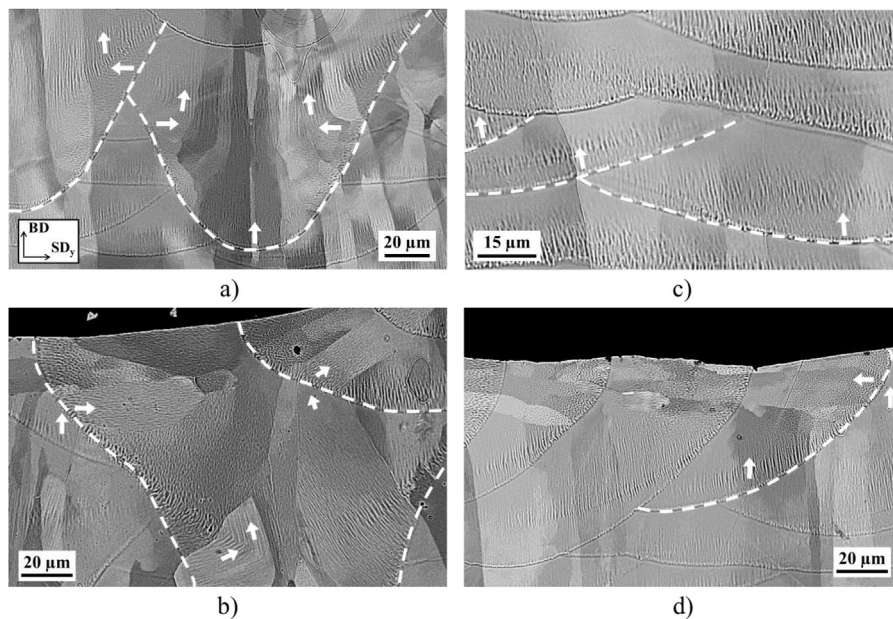

Fig. 6. Cross-sections of deep and shallow melt-pools in the sample vertical plane. The grain and solidification structures inside deep and shallow melt-pools are visible for partially remelted layers (a and c, respectively) and for the top layer (b and d, respectively). The local growth direction of the solidification structures is indicated by the arrows. The dashed lines highlight the melt-pool boundaries.

direction in Fig. 5A and B is often observed to shift by angles close to 90° in the vertical plane. In these situations the shift does not prompt the nucleation of a new grain since the grain orientation is not affected, owing to the orthogonality of the lattice vectors in the bcc crystal structure. Therefore, the existing grains can still grow across multiple melt-pools. The same mechanism is observed as the solidification structures growing from the lateral melt-pool boundaries approach the melt-pool centreline. Here, some grains are observed to shift their direction of growth abruptly by nearly

90°, as the images in Fig. 5A and B also show.

At the top layer of the parts (Fig. 6B and D), the upper portion of both the deep and shallow melt-pools is characterised by grains that have grown almost horizontally, following the direction of the solidification front, which is almost vertical in that region of the melt-pool. However, for the previous layers the upper part of the melt-pools is remelted when a new layer is deposited and therefore will disappear from the structure.

3.4. Study of crystallographic texture

EBSD data analysis shows a crystallographic texture in the grains of SLM high-silicon steel. Fig. 7 shows the resulting PFs of two different samples. These are samples S_{140} (left-hand plots) and S_{280} (right-hand plots). The PF plots quantify the texture intensities for the three crystallographic direction families <001>, <101> and <111> with respect to the front view of the sample. Both samples present a <001> texture along the BD, which is consistent with the morphological orientation of the columnar grains discussed in Section 3.3. Fig. 7 also shows that the fibre-texture in sample S_{140} is altered into a cube-texture by increasing the energy input to 280 J/m. In the cube-textured sample, the <001> axes are aligned with the BD and, in the scanning plane of the sample, with the directions running approximately halfway between the SD_x and SD_y. However, a larger spread of the texture is observed around these directions than around the BD.

The maximum texture intensity of S_{280} is found to be almost twice the maximum intensity of S_{140}. This suggests that the laser energy input largely affects the intensity of the texture, with a larger energy input producing a more textured sample.

The EBSD maps of sample S_{280} in Fig. 8 aim at providing an overview of the correlation between grain morphology and their <001> texture, both along the BD and, in the scanning plane, along the bisector of the angle between the SD_x and the SD_y. The colour-coded EBSD maps for the front view of the sample (Fig. 8A) show that the majority of the long columnar grains of sample S_{280} preferentially orient their <001> axes along the BD (left image in Fig. 8A). This result corroborates the hypothesis of epitaxial grain growth along the BD. Along the SD_x-SD_y bisector (right image in Fig. 8A), a smaller portion of the grains is red coloured.

In the horizontal plane (Fig. 8C) the majority of the grains are coloured red when the orientation of the <001> directions is considered along the BD (left image in Fig. 8C), regardless of grain morphology. Conversely, the analysis along the SD_x-SD_y bisector direction (right image in Fig. 8C) reveals that there is a correlation between the morphology of the grains and their crystallographic texture. In particular, the grains that present an equiaxed morphology in the horizontal plane tend to be characterised by a <001> texture along the BD only (fibre-texture), whereas a large portion of the elongated grains present a <001> texture both along the BD and approximately along the SD_x-SD_y bisector directions (cube-texture). The latter more or less correspond to the orientation directions of the elongated grains. The IPFs (Fig. 8B and D) are consistent with the EBSD maps in that in the scanning plane the crystallographic texture is characterised by a lower peak intensity and larger spread than along the BD.

4. Discussion

4.1. Origin of defects

It is known from the literature of SLM alloys that increasing the energy input promotes densification of the part by improving powder melting and reducing melt-pool instabilities (e.g., balling) [17–19]. However, it has been shown in Fig. 2 that while the amount of irregular porosities is reduced with the increase in energy input, the formation of the spherical pores and cracks with increasing energy input prevents the part from reaching full density. Spherical porosity formation is associated with the transition between different welding modes. The qualitative change of the melt-pool shape from flat to protuberant at high energy inputs, as shown in Fig. 2B, suggests that conduction mode welding is replaced by key-hole welding [17]. The formation of a key-hole occurs by surface vaporization of material, thus involving the creation of gas bubbles that can remain trapped inside the melt-pool during solidification. Furthermore, the dynamics of the Marangoni flow increases with laser energy input, thus increasing the probability of any gas (either newly formed or originally trapped within the highly packed powder particles) being dragged towards the bottom of the melt-pool [20].

The formation of cracks can be attributed to the thermal stresses induced during SLM processing. As presented in the literature [21], SLM introduces tensile residual stresses in the part owing to the localised application of high energy over a very short time interval (in the order of the μs) which, alongside the poor heat conductivity of the powder bed, develops a high thermal gradient around the laser spot. Differential expansion takes place and eventually the heat affected zone, whose tendency to expand is inhibited by the surrounding material, is plastically compressed. During cooling, the
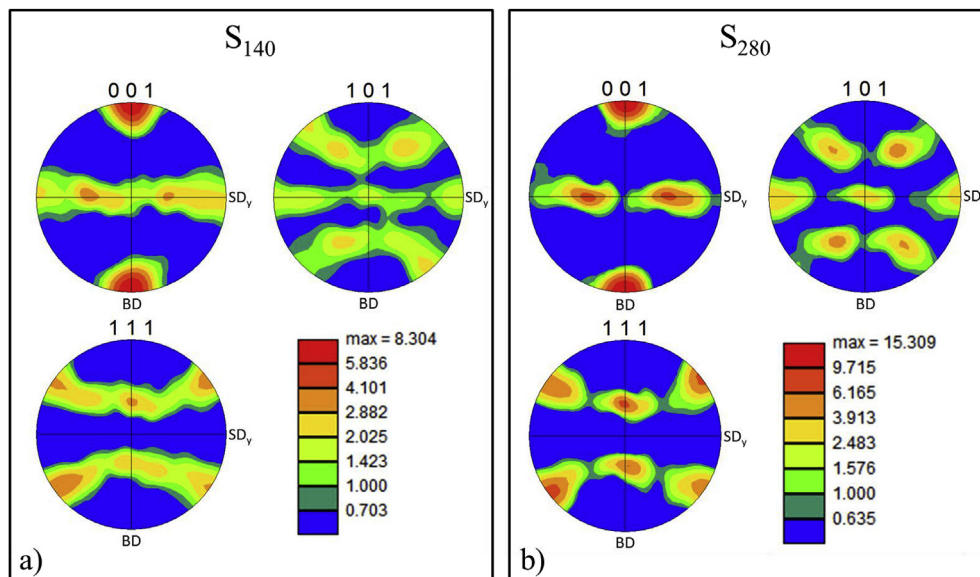

Fig. 7. Pole figures (PF) showing the preferred orientation of the <001> crystallographic direction for samples S_{280} and S_{140} and for three samples views (front, side and top).

Front View   Top View
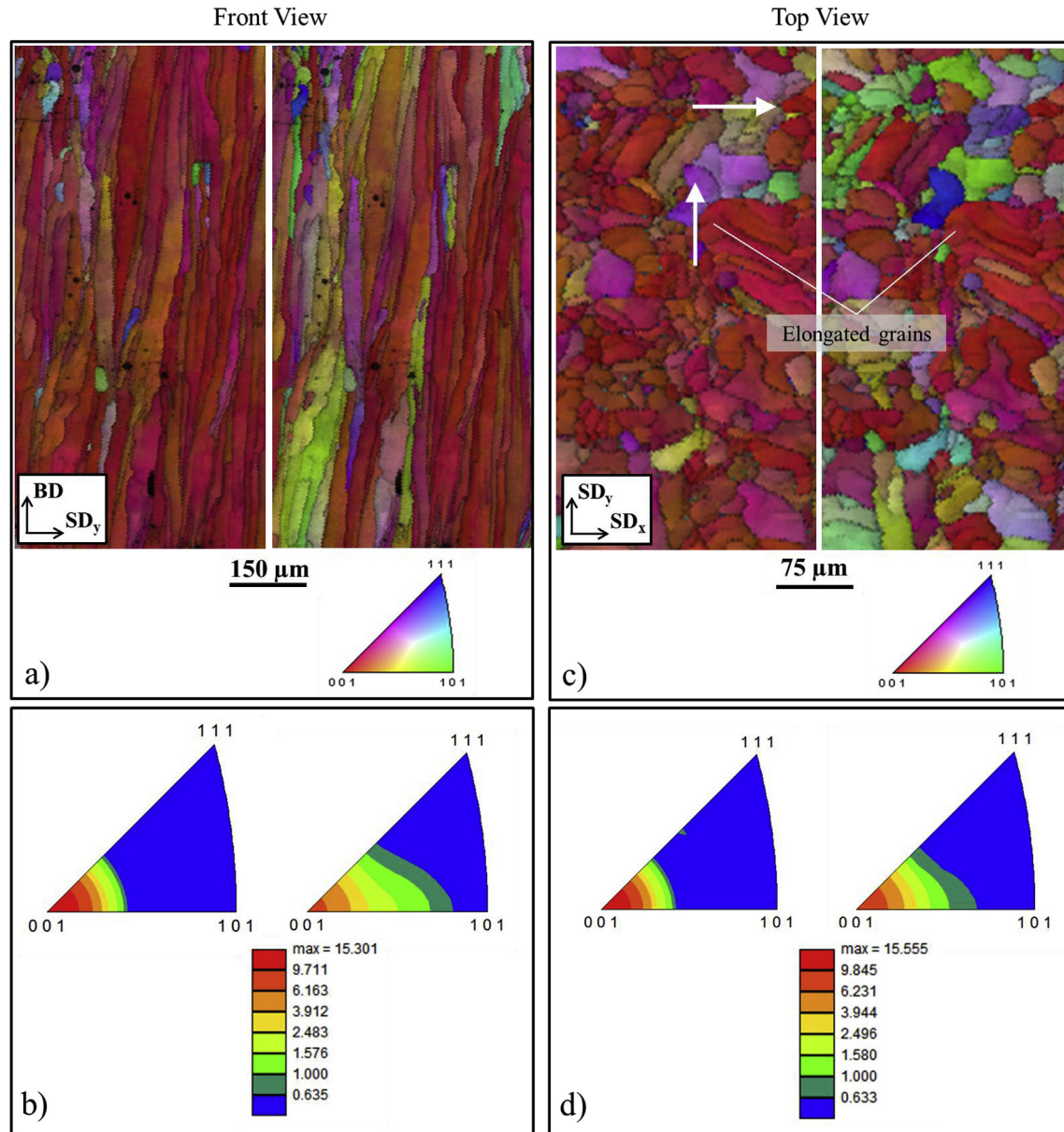

Fig. 8. EBSD maps (a and c) and IPFs (b and d) for the front and top views of sample S_{280}. The maps/IPFs on the left of each frame show the texture found along the BD. The maps and IPFs on the right of each frame show the texture along the bisector of the angle formed by SD_x and SD_y. The white arrows in the EBSD image for the top view indicate the directions of two laser scan tracks that are still visible.

upper layer's tendency to contract is again counteracted by the underlying layers, thus creating tensile stresses. In the present study, cracks propagate more or less parallel to the scanning plane (i.e., the horizontal plane), as observed in Fig. 2A. On the other hand, inter-granular crack propagation has not been observed and this is probably linked to the absence of significant macro-segregation phenomena at the grain boundaries.

4.2. Origin of solid phase formation

The results from the XRD analysis presented in Fig. 3 can be explained by considering the extremely high cooling rates (normally varying from 10^3 up to 10^6 K/s in laser welding [22]) at which the material solidifies during SLM processing. Such fast cooling, often results in non-equilibrium phase formation, i.e., the binary Fe-Si system is "frozen" into the disordered solid solution. The

order of magnitude of the cooling rates during gas-atomisation is comparable to those reached during SLM, thus explaining the relatively high lattice parameter value of the LPW powder with respect to cast Fe-6.7%Si. Literature results [23] suggest that to suppress the B_2 ordered phase when the concentration of Si is 5.6%, an average cooling rate of 340 K/s is necessary. Therefore, the high average cooling rates achieved during SLM processing can reasonably be expected to lie beyond the ordering suppression threshold.

The suppression of the ordered phases B_2 and DO_3 can be beneficial, since it makes silicon steels less brittle and electrically conductive [9,23]. The at least partial suppression of phase ordering might be another advantageous aspect of using SLM for processing high-silicon steel. However, it should be noted that XRD alone is generally not sufficient to characterise phase ordering. As discussed in section 3.3, the processed parts are characterised by fine cellular grain substructures and by visible melt-pool boundaries. These

features might indicate micro-segregation sites where intermetallic Fe_3Si could have potentially precipitated.

4.3. Origin of texture

The comparison between samples S_{140} and S_{280} has shown that doubling the laser energy input promotes columnar grain formation (Fig. 5) and intensifies the crystallographic texture along the BD (Fig. 7). The dependency of morphological and crystallographic texture intensities on laser energy input in SLM-processed parts had already been reported by the authors of [12], which found that by replacing a 400 W laser beam source with a 1000 W one, the morphological and crystallographic textures of an SLM austenitic stainless steel could be remarkably increased. The relationship can be explained by the increased amount of partial remelting and, as shown in Fig. 5, by the improved smoothness of the deposited layers. These phenomena both occur when the energy input of the scanning laser is increased. Partial remelting of the grains whose crystallographic directions of "easy growth" (the <001> family in bcc systems) orient along the BD provides a substrate for the newly processed material to solidify epitaxially, as well-known from weld metal solidification theory [22]. Clearly, a greater amount of optimally oriented grains will result in stronger texture intensities.

Fig. 7 has also shown that increasing the energy input from 140 J/m to 280 J/m also alters the <001> fibre-texture into a cubic-texture, characterised by the tendency of the <001> axes to orient both along the BD and more or less along the direction of the SD_x–SD_y bisector. This has been associated to the appearance of deeper, protuberant melt-pools, whose solidification front is almost horizontal at the melt-pool centreline, but shifts its direction towards the BD at the melt-pool sides. The protuberant melt-pool shape determines a shift in the growth direction of the cellular-dendritic solidification structures of nearly $90°$ in the vertical plane with respect to the BD, as the images in Fig. 6A and B have shown. The $90°$ shift in the growth direction is attributed to the orthogonality of the axes in the bcc system, which causes the crystallographic axis of the <001> family closer to the thermal gradient direction to be activated at the lateral boundaries of the melt-pool, thus allowing the underlying grain to grow across the melt-pool boundary horizontally.

In the scanning plane, the solidification structures that have grown almost horizontally have produced grains characterised by an elongated cross-section and oriented following the solidification front normal (refer to the grains identified by the letter E in Fig. 5). Importantly, the morphological orientation has also prompted a crystallographic texture, and the EBSD results (Figs. 7 and 8) have shown that in the scanning plane the <001> crystallographic axes tend to align along a range of directions close to the SD_x-SD_y bisector, following the morphological orientation of the grains. The formation of a cube-texture for an SLM alloy is reported in the literature [13], where it is attributed to the employment of a bidirectional X-Y scan strategy. While in the present study the formation of the cube-texture is attributed to the morphology of the melt-pool, understanding the effect of the scanning strategy on the development of the crystallographic texture would be of great interest. Unfortunately, a more extensive exploration of the effect of the SLM-process design space on the texture of the samples has been, to this date, limited by the alloy's brittle nature, which makes the creation of near-fully dense parts a challenge.

It is finally noteworthy that the nature of the specific alloy under investigation promotes texture formation, since the high silicon content suppresses γ-phase formation from the phase diagram thus leaving no secondary phase to hinder ferritic grain development.

5. Conclusions

The main findings of this research can be summarised in the following points:

- Near-fully dense high-silicon steel three-dimensional parts were manufactured using SLM for the first time in this work, starting from pre-alloyed powder;
- The SLM high-silicon steel is a single ferritic phase and super-structure lines could not be observed from the XRD measurements, suggesting the fast cooling rates of SLM retard phase ordering formation;
- The microstructure of the samples is characterised by columnar grains oriented towards the BD. Increasing the processing laser energy input seems to promote grain elongation both along the BD and in the scanning plane of the sample;
- By increasing the laser energy input, a crystallographic <001> fibre-texture can be altered into a cube-texture. This has been associated with a change in the qualitative shape of the melt-pool from shallow to protuberant.

In conclusion, this research has shown that SLM might potentially open the path to an alternative route for the manufacture of grain-oriented high-silicon steels for magnetic applications, since the <001> directions are the so-called "easy axes" of magnetisation. How the metallurgy affects the magnetic properties is the subject of ongoing research.

Acknowledgements

References

[1] N. Hopkinson, R. Hague, P. Dickens, Rapid Manufacturing: an Industrial Revolution for the Digital Age, John Wiley & Sons, 2006.

[2] M. Rombouts, J.-P. Kruth, L. Froyen, P. Mercelis, Fundamentals of selective laser melting of alloyed steel powders, CIRP Ann-Manuf Technol. 55 (2006) 187—192.

[3] L. Thijs, F. Verhaeghe, T. Craeghs, J. Van Humbeeck, J.-P. Kruth, A study of the microstructural evolution during selective laser melting of Ti—6Al—4V, Acta Mater 58 (2010) 3303—3312.

[4] B. Vandenbroucke, J.-P. Kruth, Selective laser melting of biocompatible metals for rapid manufacturing of medical parts, Rapid Prototyp. J. 13 (2007) 196—203.

[5] E. Louvis, P. Fox, C.J. Sutcliffe, Selective laser melting of aluminium components, J. Mater Process Technol. 211 (2011) 275—284.

[6] B. Zhang, N.-E. Fenineche, H. Liao, C. Coddet, Microstructure and magnetic properties of Fe—Ni alloy fabricated by selective laser melting Fe/Ni mixed powders, J Mater Sci Technol 29 (2013) 757—760.

[7] R.M. Bozorth, Ferromagnetism, Wiley-VCH, 1993.

[8] M. Namikawa, H. Ninomiya, T. Yamaji, High silicon steel sheets realizing excellent high frequency reactor performance, JFE Tech. Rep. 6 (2005) 12—17.

[9] P. Jang, B. Lee, G. Choi, Effects of annealing on the magnetic properties of Fe—6.5% Si alloy powder cores, J. Appl. Phys. 103 (2008) 07E743.

[10] H.-T. Liu, Z.-Y. Liu, Y.-Q. Qiu, Y. Sun, G.-D. Wang, Microstructure, texture and magnetic properties of strip casting Fe—6.2 wt% Si steel sheet, J. Mater Process Technol. 212 (2012) 1941—1945.

[11] X. He, X. Li, Y. Sun, Microstructure and magnetic properties of high silicon electrical steel produced by electron beam physical vapor deposition, J. Magn. Magn. Mater 320 (2008) 217—221.

[12] T. Niendorf, S. Leuders, A. Riemer, H.A. Richard, T. Tröster, D. Schwarze, Highly anisotropic steel processed by selective laser melting, Metall. Mater Trans. B 44 (2013) 794—796.

[13] L. Thijs, K. Kempen, J.-P. Kruth, J. Van Humbeeck, Fine-structured aluminium products with controllable texture by selective laser melting of pre-alloyed AlSi10Mg powder, Acta Mater 61 (2013) 1809—1819.

[14] R. Hilzinger, W. Rodewald, Magnetic materials, Vacuumschmelze, 2013.

[15] P. Beckley, Electrical Steels for Rotating Machines, IET, 2002.

[16] http://imagej.net [as on 08/02/2016].

[17] N.B. Dahotre, S. Harimkar, Laser Fabrication and Machining of Materials, Springer Science and Business Media, New York, USA, 2008.
[18] I. Yadroitsev, P. Bertrand, I. Smurov, Parametric analysis of the selective laser melting process, Appl. Surf. Sci. 253 (2007) 8064–8069.
[19] N.T. Aboulkhair, N.M. Everitt, I. Ashcroft, C. Tuck, Reducing porosity in AlSi10Mg parts processed by selective laser melting, Addit. Manuf. 1 (2014) 77–86.
[20] G. Ng, A. Jarfors, G. Bi, H. Zheng, Porosity formation and gas bubble retention in laser metal deposition, Appl. Phys. A 97 (2009) 641–649.
[21] H. Pohl, A. Simchi, M. Issa, H.C. Dias, Thermal stresses in direct metal laser sintering, in: 12th Solid Freeform Fabrication Symposium, Austin, TX, 2001.
[22] S. David, J. Vitek, Correlation between solidification parameters and weld microstructures, Int. Mater Rev. 34 (1989) 213–245.
[23] J. Shin, J. Bae, H. Kim, H. Lee, T. Lee, E. Lavernia, Z. Lee, Ordering–disordering phenomena and micro-hardness characteristics of B2 phase in Fe–(5–6.5%) Si alloys, Mater Sci. Eng. A 407 (2005) 282–290.